Simulation of ultrasonic focus aberration and correction through human tissue

Makoto Tabei
Department of Electrical and Computer Engineering, University of Rochester, Rochester, New York 14627

T. Douglas Mast[a]
Applied Research Laboratory, The Pennsylvania State University, University Park, Pennsylvania 16801

Robert C. Waag
Departments of Electrical and Computer Engineering and Radiology, University of Rochester, Rochester, New York 14627

Ultrasonic focusing in two dimensions has been investigated by calculating the propagation of ultrasonic pulses through cross-sectional models of human abdominal wall and breast. Propagation calculations used a full-wave k-space method that accounts for spatial variations in density, sound speed, and frequency-dependent absorption and includes perfectly matched layer absorbing boundary conditions. To obtain a distorted receive wavefront, propagation from a point source through the tissue path was computed. Receive focusing used an angular spectrum method. Transmit focusing was accomplished by propagating a pressure wavefront from a virtual array through the tissue path. As well as uncompensated focusing, focusing that employed time-shift compensation and time-shift compensation after backpropagation was investigated in both transmit and receive and time reversal was investigated for transmit focusing in addition. The results indicate, consistent with measurements, that breast causes greater focus degradation than abdominal wall. The investigated compensation methods corrected the receive focus better than the transmit focus. Time-shift compensation after backpropagation improved the focus from that obtained using time-shift compensation alone but the improvement was less in transmit focusing than in receive focusing. Transmit focusing by time reversal resulted in lower sidelobes but larger mainlobes than the other investigated transmit focus compensation methods. © 2003 Acoustical Society of America. [DOI: 10.1121/1.1531986]

I. INTRODUCTION

Simulation of large-scale ultrasonic propagation through realistic tissue structures has recently become feasible.[1–3] Computations of wavefront distortion produced by human abdominal wall[1,4] and breast tissue[5] models have shown the tissue models produce propagation effects similar to those measured[6–8] and has provided insight about the way various structures in tissue produce aberration.[4,9]

Simulations of ultrasonic focus aberration by tissue have previously employed models such as random phase screens[10–12] or homogeneous layers.[13–15] These models, however, do not incorporate detailed anatomic structure. Although wavefront distortion is known to limit focus and image quality,[4,10,16] further investigation of focusing is needed with more realistic models that explicitly include anatomic structure of tissue to extend current understanding.

Direct simulation of ultrasonic focusing through realistic tissue structures can elucidate the physical processes involved in ultrasonic image aberration. Of special interest is the effect of morphology on focus correction for synthetic (receive) focusing of the aberrated wavefronts in image formation[17–19] and for physical (transmit) focusing through

tissue.[20–22] Although tissue inhomogeneities are known to cause wavefront distortion and, thus, focus degradation, the relationship between specific tissue structures and focus quality has not received much attention. Transmit focus correction, in particular, has received limited previous attention in the literature, so that realistic computations of aberration-corrected transmit focusing are needed to improve understanding of transmit focus correction.

This paper presents simulations of transmit and receive focusing through two-dimensional models of abdominal wall[1,4] and breast tissue. Cylindrical wavefronts aberrated by propagation through each tissue cross section are refocused with and without correction. Focus quality is described by metrics that quantify the focal width and the relative amount of energy outside the focal region. For receive focus correction, time-shift compensation in the receiving aperture[17–19] and after backpropagation from the aperture[23,24] were employed. For transmit focus correction, these methods as well as time reversal[20] were used.

The results indicate that the quality of corrected and uncorrected focus depends on tissue type as well as the method of correction. The relative performance of correction methods for transmit and receive focusing has been shown under directly comparable conditions. In general, breast tissue in the simulations caused greater focus aberration than

---

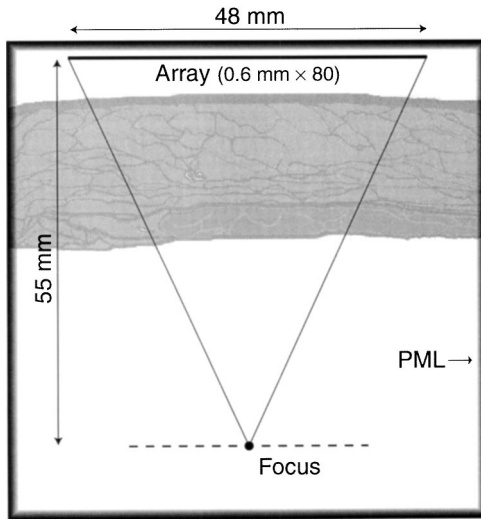[a]Present address: Ethicon Endo-Surgery, 4545 Creek Rd. ML 40, Cincinnati, OH 45242.

FIG. 1. Configuration for calculations of propagation. A virtual array, tissue model (abdominal wall A04a), and focal point are situated as shown in a 65.03×65.03 mm^2 region around which is a perfectly matched layer (PML) absorbing boundary.

abdominal wall tissue both before and after compensation. Examination of time-domain received, corrected, and focused wavefronts as well as pressure fields within tissue has provided insight into the physical basis, strengths, and limitations of each correction method. Time-shift compensation was more effective after backpropagation for both receive and transmit focusing, although this difference was smaller in the case of transmit focusing. Time reversal produced a good transmit focus due to the coherent point source employed, but was limited by spatial and temporal windowing of scattered signals as well as by frequency-dependent absorption.

II. METHODS

A. Wavefield simulations

All computations performed here used two-dimensional maps of human abdominal wall and breast tissue cross sections. The abdominal wall maps were those used in Ref. 1. The breast tissue maps were created using methods described in Ref. 1. These breast tissue maps were derived from regions of the breast where little parenchymal tissue was present so that the sections consisted primarily of fat, skin, and connective tissue. The maps represented the tissue as regions of a single tissue type: fat, muscle, or connective tissue.

The computations were performed using a virtual array, tissue map, and focal point configured as in Fig. 1. To obtain a distorted receive wavefront, a cylindrical pressure wave pulse with a sinusoidal time variation and a Gaussian envelope was propagated from a point 55 mm away to an 80-element virtual array of receivers that had a pitch of 0.60 mm and spanned 48 mm. At the start of the computations, the particle velocity was defined to be zero everywhere and the pressure distribution was defined to be

$$p(x,y;0) = e^{-[\pi b r/(2c_0)]^2/\ln(2)} J_0(2\pi f_0 r/c_0), \qquad (1)$$

TABLE I. Physical properties at 37 °C for each tissue type employed in the simulations. "CT" denotes connective tissue including septa as well as connective structures within muscle layers.

	Physical parameter				
Tissue	Sound speed mm/μs	Density g/cc	Absorption dB/(cm×MHz)	$\tau_1 = 33$ ns (κ_1/κ_∞) $\times 10^3$	$\tau_2 = 200$ ns (κ_2/κ_∞) $\times 10^3$
Water	1.524	0.993	⋯	⋯	⋯
Reference	1.524	0.993	0.50	4.32	3.64
Fat	1.478	0.950	0.52	4.36	3.67
Muscle	1.547	1.050	0.91	7.98	6.72
Skin/CT	1.613	1.120	1.61	14.72	12.40

where $r = [(x-x_0)^2 + (y-y_0)^2]^{1/2}$, the source position is (x_0, y_0), f_0 and b are the pulse center frequency and -6 dB bandwidth, respectively, and $J_0(\cdot)$ is a zeroth-order Bessel function of the first kind. This specification of the initial values corresponds to the sum of an outgoing wave and an incoming wave each band limited in temporal frequency and centered at (x_0, y_0). The starting pressure is continuous because the singularity in the temporal-frequency domain Green's function associated with the outgoing wave and used in the superposition of temporal frequencies is canceled by a corresponding singularity associated with the incoming wave. In all the simulations, f_0 was 3 MHz and b was 1.8 MHz. The array of receivers was located about 8 mm from the skin surface in the tissue map. The straight-line tissue path length from the focal or source point to the array averaged 30 mm. The source was centered in the lateral span of the array and was at least 10 mm from the other surface of the tissue map in each case. Element directivity and cross talk were emulated by integrating the pressure field over the span of each element using a trapezoidal weighting that consisted of a 0.4 mm flat region at the center and 0.2 mm linear transition that overlapped with adjacent elements on both sides.

The maps of tissue were derived from cross-sectional images that were sampled on a uniform x-y grid at 0.084 67 mm intervals (300 pixels per in.). The same grid interval was used for all the computations. Each map was used for multiple simulations by choosing sections that filled the whole computational window with a uniform thickness central portion and included no more than 25% overlap between apertures.

The tissue properties employed in the simulations are summarized in Table I. Sound speed and density values are those employed in Ref. 1. Relaxation-process absorption was implemented using two relaxation processes with compressibility parameters κ_1, κ_2 and time constants τ_1 and τ_2. The compressibility parameters and the time constants were chosen to approximate a linear dependence of absorption on frequency over the pulse bandwidth by using the formula for frequency-dependent absorption given in Ref. 25. The relaxation time constants were defined by the relations

$$\tau_1 = 1/(6f_{max}) \qquad (2a)$$

and

$$\tau_2 = 1/f_{max}, \qquad (2b)$$

where f_{max} is the nominal maximum frequency of interest. For a maximum nominal frequency that was 5.0 MHz in the simulations described here, the relaxation time constants are $\tau_1 = 33$ ns and $\tau_2 = 200$ ns. Given this choice of relaxation time constants, a reference frequency-dependent absorption of 0.50 dB/(cm·MHz) is best approximated (in a least-squares sense with an rms error of 0.02 dB/cm) for a reference density of 0.993 g/cc and a reference sound speed of 1524 mm/μs in the frequency range $1.0 < f < 5.0$ MHz by the compressibility parameters $\kappa_1 = 4.32 \times 10^{-3} \kappa_\infty$ and $\kappa_2 = 3.64 \times 10^{-3} \kappa_\infty$, where $\kappa_\infty = 1/(\rho_0 c_0^2)$ and is the compressibility of water that was 4.336×10^{-10} m·s^2/kg in the simulations. To obtain relaxation parameters for each tissue component, the coefficients were scaled using the ratio of absorption in the tissue component and the reference value and the corresponding ratio of sound speeds.

Computations were performed using a full-wave k-space method based on coupled first-order differential equations for linear acoustic propagation.[26] The method accounts for spatially-varying sound speed, density, and relaxation absorption processes, and includes perfectly matched layer (PML) absorbing boundary conditions. This method is temporally exact for homogeneous media and is also accurate for general inhomogeneous media.[26,27] The low numerical dispersion inherent to the k-space method allows the effects of frequency-dependent absorption and physical dispersion associated with relaxation-process absorption to be accurately modeled over long paths.

A grid of 768×768 points that spanned 65.03×65.03 mm^2 was used in each computation. To avoid artifactual scattering caused by boundaries between tissue types in the models,[27,28] the tissue maps were lowpass filtered using a Gaussian shaped filter with a $1/e$ response at 67% of the spatial Nyquist frequency. Density maps were shifted one-half sample in the x and y directions by shifting the phase of their spatial spectra to obtain spatial values for the staggered grid employed in the first-order k-space method.[26] The time step was 30 ns in all cases so that the Courant-Friedrichs-Lewy (CFL) number,[29] defined as $c_0 \Delta t / \Delta x$, is 0.53 for water. This choice of CFL number was sufficiently small to maintain high accuracy for the soft-tissue propagation paths considered here.[26,27]

B. Receive focusing

Waveforms received at the simulated array were corrected for geometric delay by using the known positions of the point source and aperture and the assumed sound speed in water. This removed the curvature produced by the propagation geometry and facilitated subsequent analysis of wavefront distortion as well as focusing. After geometric correction, waveforms were temporally windowed before further processing. The window was 2 μs long and had 0.5 μs cosine tapers at each end to be comparable with the window in previous simulations[1,4] and measurements.[7,8]

Wavefront distortion statistics were computed using methods analogous to those described previously.[23] For time-shift estimation, a one-dimensional version of the reference waveform method was employed to calculate the arrival time of the wavefront at each element in the simulated array. The arrival time fluctuations and their correlation length in the receiving aperture were calculated after subtracting a linear fit from the geometrically corrected wavefront, to be comparable with the fit in previous studies[1,4,7,8] that employed specimens or cross sections also with nonparallel surfaces. Wavefronts were then aligned using the computed arrival time fluctuations, and the aligned wavefronts were employed to compute energy level fluctuations, waveform similarity factor, and correlation length of the energy level fluctuations. Energy level fluctuations were defined as the sum of the squared amplitude of the waveform within the processing window, in dB units, also after removal of a linear fit. Correlation lengths were defined by the −6 dB width of the corresponding autocorrelation function. The waveform similarity factor[23] is a kind of generalized cross-correlation bounded by 0 and 1 and equal to unity when all the waveforms are identical.

The received wavefront was synthetically focused for each tissue path to obtain an image of the point source, i.e., the point-spread function for the imaging configuration. The focus was obtained using a Fourier transform implementation of the Rayleigh-Sommerfeld diffraction formula[30] in two dimensions. The implementation for a wave traveling from y_0 to y may be expressed[31]

$$p(x,y;t) = \mathrm{FT}^{-1} \left\{ e^{i(2\pi f|y-y_0|/c_0)} \int_{-\infty}^{\infty} \mathrm{FT}[p(x',y_0;t)] \right.$$
$$\left. \times \frac{|y-y_0|}{r} \pi \sqrt{f/(c_0 r)} e^{-i(2\pi f r/c_0 - \pi/4)} \, dx' \right\},$$

(3)

where

$$r = \sqrt{(x-x')^2 + (y-y_0)^2},$$

FT $[\cdot]$ is the temporal Fourier transform, and $|y-y_0|$ is the distance of propagation. The first exponential term corresponds to a time delay that centers the focused wavefront in the same 2 μs time window as the received wavefront. To ensure an acyclic temporal convolution, time sequences were zero-padded to double their size before the FFT. Use of the real-space Green's function rather than its spatial Fourier transform ensured that spatial wraparound artifacts were not a problem.[32,33] Prior to focusing, wavefronts were spatially interpolated from the step size of the element pitch (0.6 mm) to the spatial step in the simulations (0.084 67 mm). The same interpolation procedure was used for backpropagation in receive and transmit focusing along with appropriate integration to obtain waveforms at the element positions after backpropagation.

The receive focus was computed for waveforms that were uncompensated, time-shift compensated in the receive aperture, and time-shift compensated after backpropagation a distance of 40 mm. The same distance was used for all the backpropagations because trials showed the waveform similarity maximum was broad, the maximum typically occurred at a distance in the neighborhood of 40 mm, and the performance of the compensation method was not strongly dependent on the precise value of the distance.[23] In each case, a

Hamming window[34] was used to apodize the aperture before focusing. Time-shift compensation employed a sinc function multiplied by a 10-point Kaiser window[35] to interpolate amplitudes at shifts not equal to the original sampling interval. The backpropagation was performed after geometric correction, i.e., using a planar geometry.[23] Use of essentially planar wavefronts simplified the computation by eliminating the need to resample a converging wavefront on a finer spatial grid during backpropagation. Although this may seem different from physical backpropagation, a geometric acoustics argument shows that the effect of geometric correction can be represented by a scaling.[22] Propagation of a converging wave in a cylindrical geometry a distance $r_1 - r_0$ from a cylinder of radius r_1 to a cylinder of radius r_0 ($r_1 > r_0$) is equivalent to propagation in a planar geometry a distance $(r_1 - r_0)r_1/r_0$ followed by a reduction of size of the result by a factor of r_0/r_1.

C. Transmit focusing

To examine the effect of propagation through a tissue path on the transmit focus, transmit focusing was also simulated both with and without aberration correction. These simulations started with the specification of a waveform on the elements of the emulated array. The waveforms were spatially apodized with a Hamming window and geometric delays were included in the wavefront to produce a focus at a distance of 55 mm from the array. The k-space method was used to propagate the wavefront.

For transmit focusing without compensation for distortion, the unapodized waveform at the elements of the array was

$$a(t) = e^{-(\pi b t/2)^2/\ln(2)} \sin(2\pi f_0 t). \tag{4}$$

The temporal spectrum of this waveform is the same as that of the source given by Eq. (1) in the homogeneous water path region around the source. This provides a basis for comparison of transmit focuses computed using the wavefront defined by Eq. (4) with those computed using time reversal of received wavefronts.

To represent a line source extending in the x direction at the y coordinate of the array, the source term

$$s(x, t + \Delta t/2) = 2\left(\frac{c_0 \Delta t}{\Delta y}\right)\left(\frac{p(x,t) + p(x, t + \Delta t)}{2}\right) \tag{5}$$

was defined. In this expression, $p(x,t)$ is the temporal waveform $a(t)$ after apodization and inclusion of focusing delays. Equation (5) prescribes a pressure wavefront between temporal time steps as required by the k-space method using coupled first-order equations.[26] Part of this wave propagates upward (in the $-y$ direction) and part propagates downward (in the $+y$ direction) from the line source. The up-going wavefront is absorbed by the PML boundary. This specification of the source is convenient for the processing described below because the wavefield is observed as a pressure.

To compensate for changes in the apparent source amplitude for the off-axis portion of the wavefront, $p(x,t)$ was multiplied by the following obliquity factor $I(f, k_x, c_0)$ in the spatial-temporal frequency domain:

$$I(f, k_x, c_0)$$
$$= \begin{cases} [1 - (k_x c_0/(2\pi f))^2]^{1/2}, & \text{if } |k_x c_0/(2\pi f)| < 1, \\ 0, & \text{otherwise.} \end{cases} \tag{6}$$

where f is temporal frequency and k_x is the spatial frequency in the x direction. The obliquity factor allows the pressure to be used instead of the particle velocity in the Rayleigh integral.[36]

For transmit focusing that employed time-shift compensation, time shifts the same as those used for receive focus correction were applied to the waveform $a(t)$. For transmit focusing that used backpropagation, the transmit wavefront to be apodized and have focusing delays included was obtained by backpropagating a distance of 40 mm the geometrically corrected received wavefront in a 2 μs temporal window, estimating time shifts, applying these shifts to the waveform $a(t)$, and backpropagating the wavefront from the plane of the time-shift estimation to the aperture. For transmit focusing that employed time reversal, waveforms were obtained by reversing in time the waveform in a temporal 2 μs window at each element.

D. Focus evaluation

The focus was described as in Ref. 19 by an effective width in the array (x) and time (y) directions as a function of level below the peak amplitude, by a peripheral energy ratio, and by an effective radius. Effective width, defined in a given direction as the width of the maximum amplitude projection in that direction, was determined using the envelope of the analytic signal as the amplitude in the projection. The temporal effective width was converted to a spatial width using the assumed sound speed for water. Peripheral energy ratio, defined as the ratio of the pulse energy outside a reference ellipse to the pulse energy inside the ellipse, was computed at an amplitude level 10 dB below the peak. Like the reference ellipsoid used in the three-dimensional focus evaluation described in Ref. 19, the reference ellipse was centered at the position of peak amplitude. The width of the ellipse along each axis was the -10 dB effective width in the corresponding direction. The effective radius was defined as one-half the geometric mean of the effective width in the x and in the y directions.

III. RESULTS

A wavefront at an instant of time during propagation through a representative breast tissue map (B03b) from the point source is shown in Fig. 2. Visible in the wavefield are the primary cylindrical wavefront, secondary wavefronts reflected from the water-tissue boundary, and complicated scattering caused by the network of septa around lobules of subcutaneous fat in the breast. Also apparent are local time shifts in the main wavefront caused by propagation along septa aligned with the direction of propagation. These time shifts lead to interference that causes amplitude fluctuations in the received wavefront.[1]
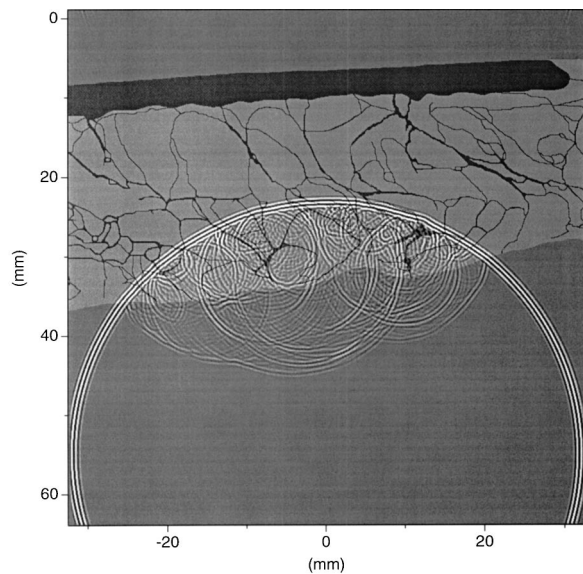
FIG. 2. A pulse wavefront at an instant of time during propagation from a point source through a representative breast tissue map (B03b). The wavefront is superimposed on the map and displayed on a 60 dB bipolar logarithmic gray scale. In the map, dark gray denotes connective tissue or skin and light gray denotes fat.

Received wavefronts are shown in Fig. 3 for a representative selection of abdominal wall and breast tissue maps. The wavefronts in the left column exhibit low arrival time and energy level fluctuations and low waveform distortion. The wavefronts in the center column have moderate arrival time and energy level fluctuations as well as moderate waveform shape distortion. The wavefronts in the right column show high arrival time and energy level fluctuations and also
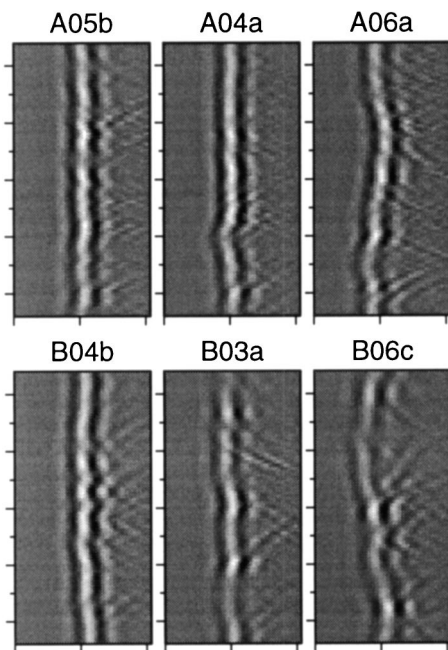

FIG. 3. Wavefronts after propagation through representative tissue maps and geometric correction. The upper row is for abdominal wall paths (from left to right: low, moderate, and high aberration), while the lower row is for breast tissue paths (from left to right: low, moderate, and high aberration). In each panel, the vertical axis spans 48 mm and the horizontal axis spans 2 μs. The amplitude gray scale is linear.

high waveform distortion. The wavefronts suggest that abdominal wall produces wavefront distortion with more small-scale spatial variation than breast, while breast produces distortion with more large-scale spatial variations than abdominal wall. The amplitude fluctuations apparent in the figure are the result of interference between distorted wavefronts as they propagate.

Statistics that describe the received wavefronts are presented in Fig. 4. The average root-mean-square (rms) arrival time fluctuation (ATF), energy level fluctuation (ELF), and ATF correlation length are about the same for both tissue paths (avg±std dev: 42.5±15.4 ns, 3.1±0.5 dB, and 4.4 ±2.7 mm, respectively, for abdominal wall and 43.9±15.2 ns, 3.3±0.8 dB, and 3.8±1.2 mm, respectively, for breast). Also for both abdominal wall and breast tissue paths, backpropagation resulted in little change of the arrival time fluctuation, energy level fluctuation, and ATF correlation length. However, the geometric scale factor discussed above is 0.58 and indicates that the true correlation lengths are much smaller (2.5 mm and 2.2 mm for abdominal wall and breast, respectively, before backpropagation). The average apparent ELF correlation length was decreased by backpropagation (from 2.3±0.4 mm to 2.0±0.3 mm for abdominal wall and from 3.3±1.5 mm to 2.7±1.0 mm for breast) but the geometric scale factor as in the case of ATF correlation lengths reduces the true length (to 1.2 mm and 1.6 mm for abdominal wall and breast, respectively). The values of waveform similarity factor (WSF) were appreciably increased and their standard deviations were decreased by backpropagation (from 0.952±0.019 to 0.978±0.008 for abdominal wall and from 0.940±0.028 to 0.975±0.014 for breast).

Wavefronts in the aperture with and without compensation and the corresponding receive focuses are illustrated in Fig. 5 for a representative highly aberrating abdominal wall path and for a representative highly aberrating breast tissue path. The wavefronts are more alike after backpropagation, as quantified by the WSF statistics plotted in the previous figure, so that backpropagation processing improves receive focusing. The focus improvement that results from backpropagation followed by time-shift compensation is greater than the improvement from time-shift compensation alone but the focus still is not ideal.

The focus improvement visible in Fig. 5 is quantified by the effective radii and peripheral energy ratios in Fig. 6 and by other receive focus statistics in Table II. The statistics for the uncompensated focus are substantially improved by time-shift compensation (TSC) and improved still further by the use of backpropagation followed by time-shift compensation (BP+TSC). For example, the mean −20 dB effective radius for breast tissue improves from 2.5±0.8 mm before compensation to 1.4±0.4 mm after time-shift compensation and to 1.2±0.4 mm after backpropagation followed by time-shift compensation. The corresponding −20 dB radius for the water path (ideal) case is 0.9 mm. In general, the statistics indicate breast causes somewhat greater receive focus degradation than abdominal wall. The breast-tissue wavefronts also focus more poorly after compensation; nevertheless, use of backpropagation processing appreciably improves the focus for the breast paths.
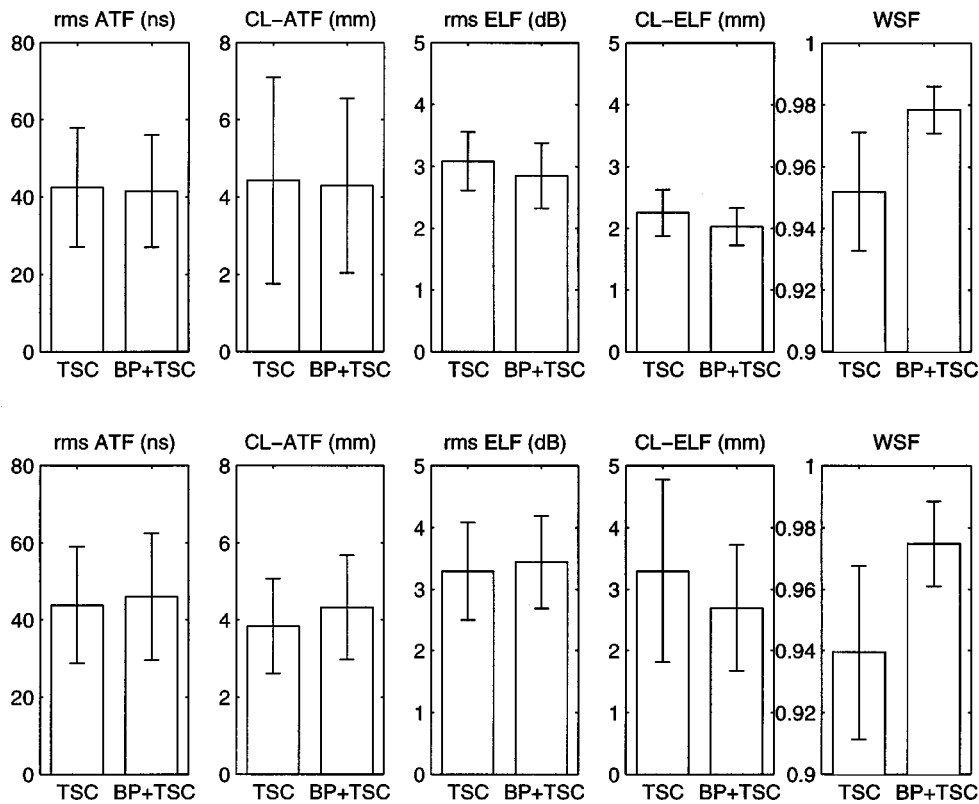
FIG. 4. Statistics of wavefronts received by a virtual array after propagation from a point source through a tissue path. The upper row shows the average and standard deviation for 12 abdominal wall paths and lower row shows the average and standard deviation for 14 breast paths. From left to right: root-mean-square (rms) arrival time fluctuation (ATF), correlation length (CL) of ATF, rms energy level fluctuation (ELF), correlation length (CL) of ELF, and waveform similarity factor (WSF). Each panel shows the results after time-shift compensation (TSC) and after backpropagation followed by time-shift compensation (BP+TSC).

The mainlobe widths of the receive focus using TSC and using BP+TSC are broader than those for the water path case. This difference arises from frequency-dependent attenuation through the tissue path. The attenuation decreases the center frequency of the received waveforms, particularly at the ends of the array and results in a smaller effective aperture. (When propagation was simulated without frequency-dependent absorption, main-lobe widths for compensated receive focusing were close to those for the ideal case.)

A converging uncompensated wavefront and secondary scattered wavefronts at an instant of time during propagation
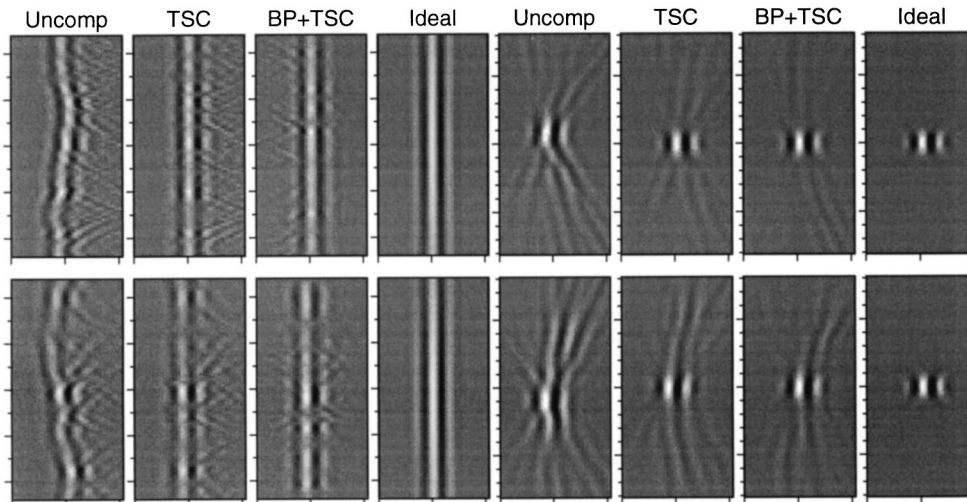

FIG. 5. Uncompensated and compensated receive wavefronts and corresponding focuses. The top row is for a representative highly aberrating abdominal wall path (A06a), while the bottom row is for a representative highly aberrating breast tissue path (B06c). The wavefronts (from left to right) are: uncompensated (Uncomp), time-shift compensated (TSC), backpropagated and time-shift compensated (BP+TSC), and water path (Ideal), respectively, and the corresponding focused wavefronts. The vertical axis spans 48 mm for wavefronts in the aperture and 16 mm for the focused wavefronts, while the horizontal axis spans 2 μs in each case. The amplitude gray scale is linear.
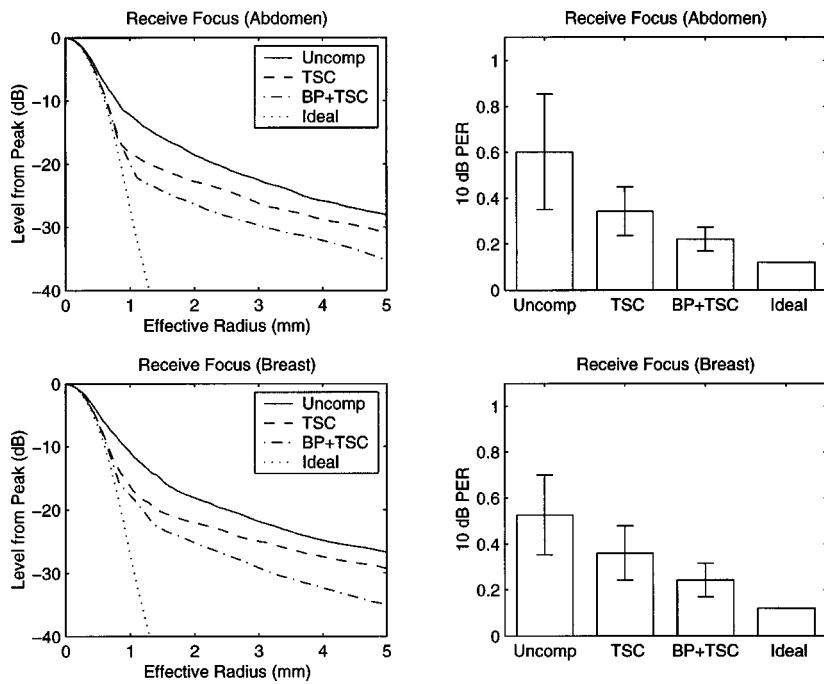
FIG. 6. Effective width and peripheral energy ratio (PER) for receive focusing. The upper panels show the average for 12 abdominal wall paths and the lower panels show the average for 14 breast tissue paths. Uncomp =uncompensated, TSC=time-shift compensation, BP+TSC=backpropagation followed by time-shift compensation, Ideal=water path.

through a representative breast tissue map from the virtual array is shown in Fig. 7. The relatively large element size (0.6 mm, 1.2 times the wavelength at the 3 MHz center frequency) results in grating-lobe wavefronts that appear as curved lines at the sides of the converging wavefront. However, these wavefronts dissipate as the main wavefront approaches the focus. As in the case of propagation from a point source, scattering occurs as the wavefront strikes boundaries between different tissue components.

Transmit wavefronts without and with compensation (before the addition of geometric delay in each case) in the emulated aperture and the corresponding transmit focuses after propagation through a representative highly aberrating abdominal wall and a representative highly aberrating breast tissue path are shown in Fig. 8. The uncompensated transmit focuses show aberration similar to the uncompensated receive focuses even though the focusing processes are differ-

ent. Compared to time-shift compensation with and without backpropagation, the focus resulting from time-reversal has a broader mainlobe as a consequence of the apodization and has lower sidelobes as a consequence of the relatively weak inhomogeneity of the attenuation and the invariance of lossless propagation to the direction of time.

In contrast to receive focus correction that removes distortion from the wavefront, transmit focus correction predistorts or modifies the wavefront to include a kind of distortion in the transmitted wavefront. Although the focus resulting from time-shift compensation of the backpropagation is improved over the focus resulting from time-shift compensation alone, the improvement is smaller than in receive focusing. As in receive focusing, breast caused greater degradation than abdominal wall. This is expected from the greater amplitude fluctuations in the BP+TSC and time reversed wavefronts.

TABLE II. -10 dB and -20 dB effective radii (ER) in mm and -10 dB peripheral energy ratios (PER) for simulated focusing. Effective widths and peripheral energy ratios are shown for breast and abdominal wall tissue simulations of transmit (TX) and receive (RX) focusing with wavefronts that were uncompensated (Uncomp), time-shift compensated (TSC), time-shift compensated after backpropagation (BP+TSC), or time reversed (TR). Each statistic is shown using the format mean±standard deviation.

| Statistic	Focus	Tissue	Uncomp	TSC	BP+TSC	TR
-10 dB	RX	Abdomen	0.80±0.18	0.64±0.02	0.64±0.01	⋯
ER		Breast	0.92±0.30	0.66±0.03	0.64±0.02	⋯
	TX	Abdomen	0.78±0.15	0.62±0.01	0.63±0.01	0.65±0.02
		Breast	0.93±0.35	0.65±0.07	0.64±0.04	0.65±0.03
-20 dB	RX	Abdomen	2.33±0.80	1.29±0.33	1.01±0.22	⋯
ER		Breast	2.51±0.80	1.43±0.43	1.20±0.36	⋯
	TX	Abdomen	2.34±0.79	1.32±0.44	1.24±0.40	0.98±0.08
		Breast	4.32±2.75	2.40±1.51	2.09±1.33	1.57±0.93
-10 dB	RX	Abdomen	0.60±0.25	0.34±0.11	0.22±0.05	⋯
PER		Breast	0.53±0.17	0.36±0.12	0.24±0.07	⋯
	TX	Abdomen	0.70±0.22	0.48±0.16	0.41±0.11	0.27±0.06
		Breast	0.78±0.29	0.63±0.27	0.53±0.22	0.36±0.14
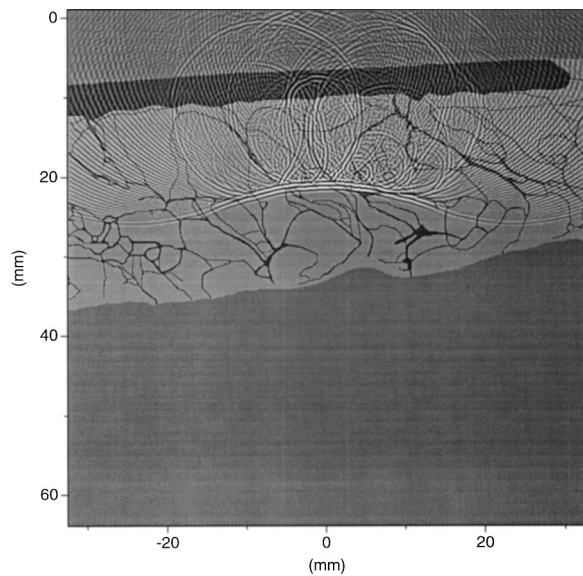
FIG. 7. A converging uncompensated pulse wavefront and secondary scattered wavefronts at an instant of time during propagation from a virtual array through a representative breast tissue map (B03b). The wavefront is superimposed on the map and displayed on a 60 dB bipolar logarithmic gray scale. In the map, dark gray denotes connective tissue or skin and light gray denotes fat.

Statistics of the transmit focuses are shown in Fig. 9 as well as in Table II. The transmit focus quality is generally similar to that for receive focusing in the case of abdominal wall. However, the size of the focus as quantified by the -20 dB effective radii shown in Table II is much larger for transmit focusing through breast tissue than for receive focusing (e.g., 4.3 ± 2.8 mm vs 2.5 ± 0.8 mm uncompensated and 2.4 ± 1.5 mm vs 1.4 ± 0.4 mm using time-shift compensation). As expected from the representative focuses shown in Fig. 8, BP+TSC produces a smaller improvement over TSC, in contrast to receive focusing where significant improvement is evident. Also, as seen from comparison of the -10 dB effective radii in Table II, the mainlobe for time-reversal focusing is wider than for TSC and BP+TSC correction. This occurs for two main reasons. First, the received wavefront has undergone frequency-dependent absorption during propagation through the tissue and, consequently, the waveform is lengthened and the wavefront amplitude is further reduced by a longer attenuating path to the edges of the aperture. Second, the spatial weighting of the time-reversed wavefront by the product of the cylindrical spreading factor $1/\sqrt{r}$ and the Hamming window reduces the effective size of the aperture. Nevertheless, the time reversal procedure yields a good focus, at least for the case in which a wavefront from a point source is available. Once again, the degradation caused by the breast tissue is larger than that from abdominal wall tissue, both before and after compensation. These differences are larger for transmit focusing than for receive focusing.

IV. DISCUSSION

The ATF values in the current simulations are about 20% smaller than those in previous simulations[1,4] that employed plane wave propagation. This decrease is attributed mainly to the difference in geometry between point-source and plane-wave propagation. During propagation from the point source, the wavefronts pass through a region that is narrow near the source and widens toward the array so the wavefront encounters fewer different inhomogeneities while passing through the tissue. The values of ATF in simulations of propagation through tissue are much smaller than the corresponding values in measurements because, as previously discussed,[1,4] the tissue maps are less complicated than tissue and propagation is physically different in two and three dimensions.

The ELF values are about the same as those in previous simulations[1,4] and measurements[7] using abdominal wall and about 1 dB less than measurements[8] using breast. The similarity of values is attributed mostly to the local nature of the energy level fluctuations. The short-range correlation is not greatly affected by the fitting process that employed a linear
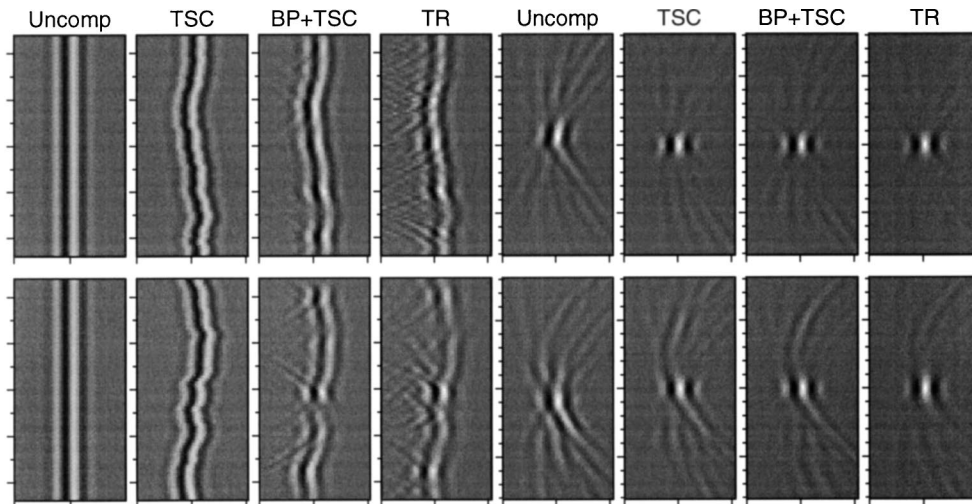

FIG. 8. Uncompensated and compensated transmit wavefronts and corresponding focuses. The top row is for a representative highly aberrating abdominal wall path (A06a), while the bottom row is for a representative highly aberrating breast tissue path (B06c). The wavefronts (from left to right) are: uncompensated (Uncomp), time-shift compensated (TSC), backpropagated and time-shift compensated (BP+TSC), and time reversed (TR), and the corresponding focused wavefronts. The vertical axis spans 48 mm for wavefronts in the aperture and 16 mm for the focused wavefronts, while the horizontal axis spans 2 μs in each case. The amplitude gray scale is linear.
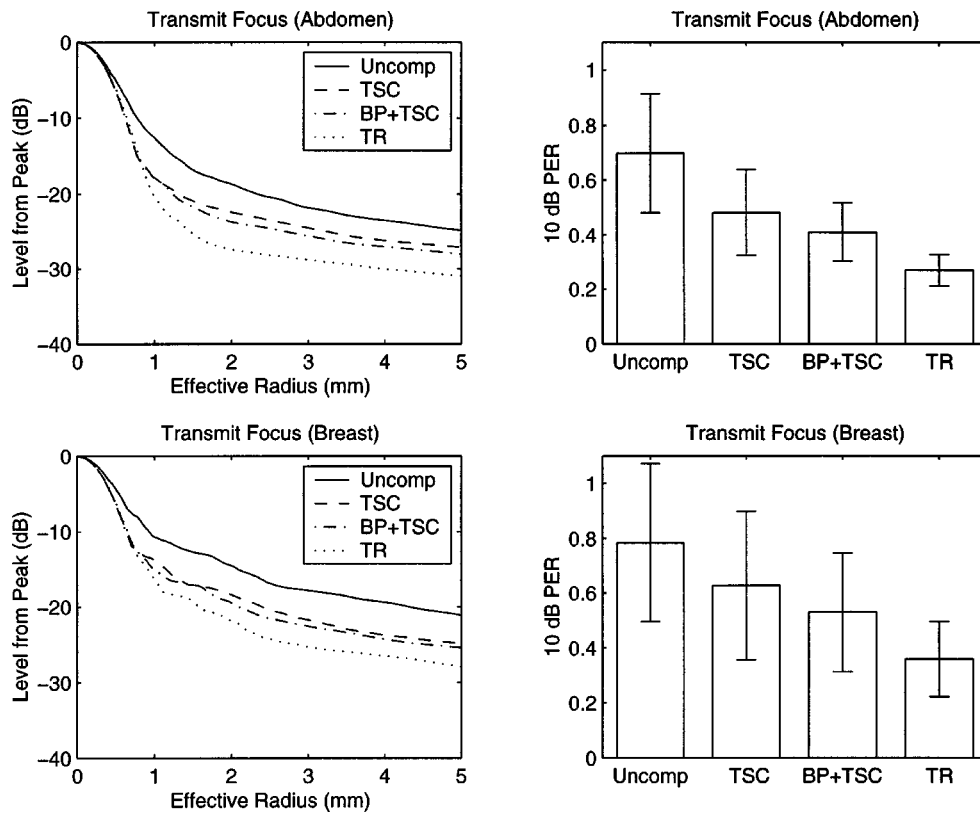
FIG. 9. Effective beam width and peripheral energy ratio (PER) for transmit focusing. The upper panels show the average for 12 model abdominal wall paths and lower panels show the average for 14 model breast tissue paths. The line convention is the same as in Fig. 6 except that TR=time reversal.

fit in the referenced (two-dimensional) simulations of plane-wave propagation through tissue cross sections and a fourth-order, two-dimensional polynomial fit in the referenced measurements of point-source (three-dimensional) propagation through tissue specimens.

The statistics of receive focus metrics agree, however, qualitatively with those obtained from measurements of breast[8] and abdominal wall tissue,[23] although the skirts of the receive focus effective-radius curves are higher in the present study. A major reason for this is that sidelobes decay more slowly in a two-dimensional focus compared to those in a three-dimensional focus. However, waveform similarity factors and energy level fluctuations have similar values to those in Ref. 23 and improvement before and after back-propagation processing is similar to that in Ref. 23 as well. These observations indicate that the distortion simulated here is similar to that measured in human tissue Refs. 8 and 23 even though the arrival-time and energy-level fluctuations differ due to differences in geometry.

The investigated compensation methods performed better for receive focusing than for transmit focusing. Although effective radii for uncompensated focusing are almost identical down to -17 dB for abdominal wall paths and -12 dB for breast tissue paths, effective radii at lower levels are wider for the transmit case. Peripheral energy ratios are also substantially higher for uncompensated transmit focusing. The values of these two metrics indicate higher sidelobe levels compared to receive focusing. Furthermore, backpropagation followed by time-shift compensation in transmit focus correction showed less improvement over time-shift com-

pensation alone than in receive focus correction. This observation agrees with a corresponding observation in an experimental study[22] that employed a two-dimensional array.

The difference between receive and transmit focus improvement is attributed primarily to the difference of the estimation process using homogeneous medium and physical propagation through distributed inhomogeneities. In compensation during reception, the homogeneous path assumed in estimation is also used in focusing. In compensation during transmission, however, the path used for estimation is different from the physical path used for transmission. Although this process works well for a phase screen or a very thin layer of aberration, the performance is degraded as the thickness of aberrating medium increases.

Focus compensation employing backpropagation produces edge waves that merit comment. These edge waves affect the estimation of time-shifts at the boundary of the aperture. In receive focusing, apodization reduces the influence of any time-shift errors and the receive focus improvement that results from inclusion of the backpropagation step before time-shift estimation is appreciable. In transmit focusing, the edge waves depend on the way the compensation is implemented. For example, instead of time-shifting a specific pulse waveform to obtain the wavefront that is backpropagated from the position of the time-shift screen to the position of the aperture and then apodizing the resulting wavefront in the aperture as in the studies described here, the wavefront that is time-shifted can be obtained by backpropagation of an already apodized wavefront from the transmit aperture as in Ref. 22. This latter procedure reduces the edge

Tabei *et al.*: Simulation of ultrasonic focusing

waves in the backpropagation from the position of the phase screen but residual edge effects remain along the inner border of the transmit aperture. Since trials showed the transmit focus is about the same using each implementation and since shifting a given pulse at the position of the phase screen is straightforward and requires less computation, that method was used here.

A comparison of time reversal and backpropagation followed by time-shift compensation provides insight about the limited improvement in transmit focusing provided by backpropagation followed by time-shift compensation. While time reversal implicitly incorporates distortion effects along the entire propagation path, the backpropagation processing employed here effectively concentrates distributed aberration in a single phase screen at the backpropagation distance. Although wavefronts compensated using backpropagation processing appear similar to time-reversed wavefronts as seen in Fig. 8, the time-reversed wavefronts contain larger amplitude fluctuations. The smaller amplitude fluctuations produced by backpropagation are insufficient to compensate fully for amplitude variations caused by the distributed inhomogeneities.

The time-reversal method for transmit focusing through the realistic tissue paths used in this study did not approach an ideal diffraction-limited focus. The performance of time-reversal compensation is affected by irreversible processes that exist in practice. Important among these are absorption, element directivity, finite time window, and scattering loss. Also, propagation of a prefocused wavefront serves better than the point source because less energy is lost outside the receive aperture. Although all effects other than scattering loss may be removed in simulations to improve the performance of time-reverse compensation significantly, this has not been done because changes were not used with other methods and a fair comparison of methods under similar practical circumstances is the goal here.

One may ask how well time-reversal processing can perform in practice with finite apertures and temporal windows. The answer is apparently that as long as a point source is available at the focus, time-reversal compensation is superior to the investigated compensation methods in sidelobe suppression though the difference may be reduced depending on physical constraints. This good performance is likely because the time-reversed wavefront still contains some information associated with secondarily scattered and refracted wavefronts. However, in most practical cases, point sources are not available.

The backpropagation method has the advantage of not requiring a point source. The time-reversal method, however, requires at least a pointlike source. Although the difficulty of time-shift estimation from diffuse scattering may slightly increase due to reduced coherence, time-shift estimation in this setting is not a significant problem.[37]

In the realistic situations, further improvement of transmit focus quality is also possible using a spatio-temporal inverse filter.[38] This has been shown to provide a better focus than time reversal in an inhomogeneous medium with attenuation.[39] However, the inverse filtering in this method requires received wavefronts for multiple, well-defined source locations, a configuration not possible in most practical pulse-echo medical imaging applications. Nevertheless, if accurate tissue models are available, simulations like those presented here may be useful in the development of new methods for transmit focus correction.

Notable is that the present simulations, which employed two-dimensional cross-sectional models of breast and abdominal wall tissue, may somewhat underestimate the focus degradation caused by human tissue. As generally understood[40] and recently shown for human breast-tissue simulations,[5] propagation through three-dimensional inhomogeneous media causes greater distortion than propagation through two-dimensional models of the same media. Thus, two-dimensional simulations are expected to result in less focus degradation. However, as discussed above, a two-dimensional focus has higher sidelobe levels than a three-dimensional focus so that this difference may be diminished.

In general, breast tissue causes larger aberration than abdominal tissue. However, the aberration appears at relatively lower spatial frequencies. This may explain why commercial scanners operating at a higher frequency and using a higher f-number than employed in this study are more effective in breast imaging than in abdominal imaging. In addition, the adverse effects of aberration on high-frequency breast imaging may be partially compensated by use of tissue compression and selection of transducer position for optimal image quality.

Overall, despite simplifications associated with the tissue model and with propagation in two dimensions, the qualitative agreement of results in this study with results from measurements and the realistic appearance of the wavefront distortion and focus aberration in this study show the employed combination of the tissue maps and k-space method of calculation is useful for investigation of focusing and aberration correction in ultrasonic applications through a tissue path.

V. CONCLUSIONS

Simulations employing cross-sectional models of human abdominal wall and breast tissue have provided new information about the effects of tissue structure and compensation on receive and transmit focusing in medical ultrasound. The receive and transmit focus degradation caused by breast tissue were greater than those caused by abdominal wall before and after compensation. The quality of the transmit focus obtained through breast tissue was particularly low. This is attributed to the large amplitude fluctuations caused by large-scale connective tissue structures in breast tissue.

Aberration correction for receive focusing was effective both for abdominal wall and breast tissue paths, although focus quality remained lower for breast after compensation. Time-shift compensation significantly improved focusing but time-shift compensation after backpropagation was substantially better. Since the receive focus can be considered a point-spread function of an analogous imaging system, these results indicate that aberration correction can, in principle, greatly improve the quality of images obtained through tissue paths with large-scale distributed inhomogeneities, provided a satisfactory estimate of the aberration can be obtained.

J. Acoust. Soc. Am., Vol. 113, No. 2, February 2003

Tabei *et al.*: Simulation of ultrasonic focusing 1175

The improvement of transmit focusing by the methods studied was not as great as obtained in receive focusing. In particular, time-shift compensation after backpropagation provided only small improvement over time-shift compensation alone. Time-reversal produced a transmit focus with low sidelobe levels but a wider mainlobe relative to the other compensation methods investigated and was apparently limited by a smaller effective aperture and spatially varying, frequency-dependent attenuation.

[1] T. D. Mast, L. M. Hinkelman, M. J. Orr, V. W. Sparrow, and R. C. Waag, "Simulation of ultrasonic pulse propagation through the abdominal wall," J. Acoust. Soc. Am. **102**, 1177–1190 (1997). [Erratum: J. Acoust. Soc. Am. **104**, 1124–1125 (1998).]

[2] G. Wojcik, B. Fornberg, R. Waag, L. Carcione, J. Mould, L. Nikodym, and T. Driscoll, "Pseudospectral methods for large-scale bioacoustic models," 1997 IEEE Ultrason. Symp. Proc. **2**, 1501–1506 (1997).

[3] J. L. Aroyan, "Three-dimensional modeling of hearing in *Delphinus delphis*," J. Acoust. Soc. Am. **110**, 3305–3318 (2001).

[4] T. D. Mast, L. M. Hinkelman, M. J. Orr, and R. C. Waag, "The effect of abdominal wall morphology on ultrasonic pulse distortion. Part II. Simulations," J. Acoust. Soc. Am. **104**, 3651–3664 (1998).

[5] T. D. Mast, "Two- and three-dimensional simulations of ultrasonic propagation through human breast tissue," Acoust. Res. Lett. Online **3**, 53–58 (2002).

[6] Q. Zhu and B. D. Steinberg, "Large-transducer measurements of wavefront distortion in the female breast," Ultrason. Imaging **14**, 276–299 (1992).

[7] L. M. Hinkelman, D-L. Liu, L. A. Metlay, and R. C. Waag, "Measurements of ultrasonic pulse arrival time and energy level variations produced by propagation through abdominal wall," J. Acoust. Soc. Am. **95**, 530–541 (1994).

[8] L. M. Hinkelman, D.-L. Liu, R. C. Waag, Q. Zhu, and B. D. Steinberg, "Measurement and correction of ultrasonic pulse distortion produced by the human breast," J. Acoust. Soc. Am. **97**, 1958–1969 (1995).

[9] T. D. Mast, L. M. Hinkelman, L. A. Metlay, and R. C. Waag, "The effect of abdominal wall morphology on ultrasonic pulse distortion. Part I. Measurements" J. Acoust. Soc. Am. **104**, 3635–3649 (1998).

[10] G. E. Trahey, P. D. Freiburger, and D. C. Sullivan, "The impact of acoustic velocity variations on target detectability in ultrasonic images of the breast," Invest. Radiol. **26**, 782–791 (1991).

[11] A. P. Berkhoff and J. M. Thijssen, "Correction of concentrated and distributed aberrations in medical ultrasound imaging," 1996 IEEE Ultrason, Symp. Proc. **2**, 1405–1410 (1996).

[12] T. Christopher, "Finite amplitude distortion-based inhomogeneous pulse echo ultrasonic imaging," IEEE Trans. Ultrason. Ferroelectr. Freq. Control **44**, 125–139 (1997).

[13] L. Ødegaard, E. Halvorsen, B. Ystad, H. G. Torp, and B. A. Angelsen, "Delay and amplitude focusing through the body wall; A simulation study," 1996 IEEE Ultrason. Symp. Proc. **2**, 1411–1414 (1996).

[14] I. M. Hallaj and R. O. Cleveland, "FDTD simulation of finite-amplitude pressure and temperature fields for biomedical ultrasound," J. Acoust. Soc. Am. **105**, L7–L12 (1999).

[15] P. Roux, H. C. Song, M. B. Porter, and W. A. Kuperman, "Application of the parabolic equation method to medical ultrasonics," Wave Motion **31**, 181–196 (2000).

[16] Q. Zhu, B. D. Steinberg, and R. L. Arenson, "Wavefront amplitude distortion and image sidelobe levels: Part II—*in vivo* experiments," IEEE Trans. Ultrason. Ferroelectr. Freq. Control **40**, 754–762 (1993).

[17] M. O'Donnell and S. W. Flax, "Phase-aberration correction using signals from point reflectors and diffuse scatterers: Measurements," IEEE Trans. Ultrason. Ferroelectr. Freq. Control **35**, 768–774 (1988).

[18] L. Nock, G. E. Trahey, and S. W. Smith, "Phase aberration correction in medical ultrasound using speckle brightness as a quality factor," J. Acoust. Soc. Am. **85**, 1819–1833 (1989).

[19] D.-L. Liu and R. C. Waag, "Time-shift compensation of ultrasonic pulse focus degradation using least-mean-square error estimates of arrival time," J. Acoust. Soc. Am. **95**, 542–555 (1994).

[20] M. Fink, "Time-reversal of ultrasonic fields—Part I: Basic principles," IEEE Trans. Ultrason. Ferroelectr. Freq. Control **39**, 555–567 (1992).

[21] H. Wang, E. S. Ebbini, M. O'Donnell, and C. A. Cain, "Phase aberration correction and motion correction for ultrasonic hyperthermia phased arrays: Experimental results," IEEE Trans. Ultrason. Ferroelectr. Freq. Control **41**, 34–43 (1994).

[22] J. C. Lacefield and R. C. Waag, "Evaluation of backpropagation methods for transmit focus compensation," 2001 IEEE Ultrason. Symp. Proc., paper 2D-4 (2001).

[23] D.-L. Liu and R. C. Waag, "Correction of ultrasonic wavefront distortion using backpropagation and a reference waveform method for time-shift compensation," J. Acoust. Soc. Am. **96**, 649–660 (1994).

[24] C. Dorme and M. Fink, "Ultrasonic beam steering through inhomogeneous layers with a time reversal mirror," IEEE Trans. Ultrason. Ferroelectr. Freq. Control **43**, 167–175 (1996).

[25] A. I. Nachman, J. F. Smith, and R. C. Waag, "An equation for acoustic propagation in inhomogeneous media with relaxation losses," J. Acoust. Soc. Am. **88**, 1584–1595 (1990).

[26] M. Tabei, T. D. Mast, and R. C. Waag, "A *k*-space method for coupled first-order acoustic propagation equations," J. Acoust. Soc. Am. **111**, 53–63 (2002).

[27] T. D. Mast, L. P. Souriau, D.-L. D. Liu, M. Tabei, A. I. Nachman, and R. C. Waag, "A *k*-space method for large-scale models of wave propagation in tissue," IEEE Trans. Ultrason. Ferroelectr. Freq. Control **48**, 341–354 (2001).

[28] J. C. Mould, G. L. Wojcik, L. M. Carcione, M. Tabei, T. D. Mast, and R. C. Waag, "Validation of FFT-based algorithms for large-scale modeling of wave propagation in tissue," 1999 IEEE Ultrason. Symp. Proc. **2**, 1551–1556 (1999).

[29] E. Turkel, "On the practical use of high-order methods for hyperbolic systems," J. Comput. Phys. **35**, 319–340 (1980).

[30] J. W. Goodman, *Introduction to Fourier Optics* (McGraw-Hill, New York, 1968), Sec. 3.4.

[31] P. M. Morse and K. U. Ingard, *Theoretical Acoustics* (McGraw-Hill, New York, 1968), Sec. 7.3.

[32] M. Tabei and M. Ueda, "On the sampling conditions for reconstruction of an acoustic field from a finite sound source," J. Acoust. Soc. Am. **111**, 940–946 (2002).

[33] R. C. Waag, J. A. Campbell, J. Ridder, and P. R. Mesdag, "Cross-sectional measurements and extrapolations of ultrasonic fields," IEEE Trans. Sonics Ultrason. **SU-32**, 26–35 (1985).

[34] R. B. Blackman and J. W. Tukey, *The Measurement of Power Spectra* (Dover, New York, 1958), Sec. II B 5.

[35] A. V. Oppenheim and R. W. Schafer, *Discrete-Time Signal Processing* (Prentice Hall, Englewood Cliffs, NJ, 1989), Sec. 7.4.

[36] A. D. Pierce, *Acoustics: An Introduction to Its Physical Principles and Applications* (McGraw-Hill, New York, 1981), Sec. 5.2.

[37] D.-L. D. Liu and R. C. Waag, "Estimation and correction of ultrasonic wavefront distortion using pulse-echo data received in a two-dimensional aperture," IEEE Trans. Ultrason. Ferroelectr. Freq. Control **45**, 473–490 (1998).

[38] M. Tanter, J.-F. Aubry, J. Gerber, J.-L. Thomas, and M. Fink, "Optimal focusing by spatio-temporal inverse filter. I. Basic principles," J. Acoust. Soc. Am. **110**, 37–47 (2001).

[39] J.-F. Aubry, M. Tanter, J. Gerber, J.-L. Thomas, and M. Fink, "Optimal focusing by spatio-temporal inverse filter. II. Experiments. Application to focusing through absorbing and reverberating media," J. Acoust. Soc. Am. **110**, 48–58 (2001).

[40] J. M. Martin and S. M. Flatté, "Simulation of point-source scintillation through three-dimensional random media," J. Opt. Soc. Am. A **7**, 838–847 (1990).